Faraday Discussions

Cite this: *Faraday Discuss.*, 2023, **242**, 129

ROYAL SOCIETY OF CHEMISTRY

PAPER

View Article Online
View Journal | View Issue

Synthesis and structural properties of high-entropy nanoalloys made by physical and chemical routes†

Andrea Barbero,[a] Cora Moreira Da Silva,[b] Nathaly Ortiz Pena,[a] Nour Kefane,[b] Abdallah Jaafar,[a] Maxence Thorey,[a] Hicham Bouaia,[a] Jaysen Nelayah,[a] Guillaume Wang,[a] Hakim Amara,[ac] Christian Ricolleau,[a] Vincent Huc[b] and Damien Alloyeau *[a]

Received 23rd May 2022, Accepted 18th July 2022
DOI: 10.1039/d2fd00118g

The development of synthesis methods with enhanced control over the composition, size and atomic structure of High Entropy Nano-Alloys (HENA) could give rise to a new repertoire of nanomaterials with unprecedented functionalities, notably for mechanical, catalytic or hydrogen storage applications. Here, we have developed two original synthesis methods, one by a chemical route and the other by a physical one, to fabricate HENA with a size between 3 and 10 nm and a face centered cubic structure containing three (CoNiPt), four (CoNiPtCu and CoNiPtAu) or five (CoNiPtAuCu) metals close to the equiatomic composition. The key point in the proposed chemical synthesis method is to compensate the difference in reactivity of the different metal precursors by increasing the synthesis temperature using high boiling solvents. Physical syntheses were performed by pulsed laser ablation using a precise alternating deposition of the individual metals on a heated amorphous carbon substrate. Finally, we have exploited aberration-corrected transmission electron microscopy to explore the nanophase diagram of these nanostructures and reveal intrinsic thermodynamic properties of those complex nanosystems. In particular, we have shown (i) that the complete mixing of all elements can only occur close to the equiatomic composition and (ii) how the Ostwald ripening during HENA synthesis can induce size-dependent deviations from the equiatomic composition leading to the formation of large core–shell nanoparticles.

[a]*Université Paris Cité, CNRS, Laboratoire Matériaux et Phénomènes Quantiques, 75013 Paris, France. E-mail: damien.alloyeau@u-paris.fr; Tel: +33 (1) 57 27 69 83*
[b]*Laboratoire d'Etude des Microstructures, ONERA – CNRS, Chatillon, France*
[c]*Institut de Chimie Moléculaire et des Matériaux d'Orsay, Université de Paris Saclay – CNRS, Orsay, France*
† Electronic supplementary information (ESI) available. See https://doi.org/10.1039/d2fd00118g

1. Introduction

High entropy alloys (HEA) have become one of the most popular material classes in the last decades in both fundamental and applied materials science. This new concept allows the fabrication of many alloys mixing four to eight metals in a cubic solid solution with promising and tunable mechanical and catalytic properties.[1,2] While much research has mostly been focused on exploring the compositional space of bulk HEA, the possibility to tune alloy properties with size effects has until recently been ignored because of the absence of well-controlled methods to synthesize HEA nanoparticles (NPs). In the last three years, some studies have shown that high entropy nano-alloys (HENA) can be fabricated using high temperature techniques such as carbothermal shock,[3] fast moving bed pyrolysis,[4] mechanical ball milling[5] or plasma arc discharge,[6] but the simultaneous control over both the composition and the size of HEA NPs remains limited and the crucial interplay between the size, composition and atomic structure of these new nanosystems has hardly been addressed.[7] Moreover, the extreme conditions of these syntheses are not suitable to expect the use of these NPs in various industrial applications.[8] Yet the game is worth the effort, because the development of synthesis methods where elemental composition, atomic structure and particle size are precisely controlled could bring an additional degree of freedom to design new materials.[9] For example, the increase in mechanical strength associated with size reduction in most metals could be exploited together with the enhanced mechanical properties of HEA in structure materials.[10,11] Moreover, the high specific surface area and the existence of a large number of active sites with diverse atomic arrangements at the surface of HENA could lead to new classes of materials for heterogeneous (electro-)catalysis,[12–17] gas sensing,[18] corrosion resistant coating[5,19] or hydrogen storage applications.[20] In this work, the target HENA are CoPtNiCuAu NPs and their subsets. This system has several advantages for establishing a robust, step-by-step research approach to achieve a perfectly controlled synthesis. Indeed, this particular alloy, based on individual elements all crystallizing into a face centred cubic (FCC) structure at nanoscale, can be divided into subsets of sub-binary systems with tendencies towards both chemical ordering (CoPt, PtNi, CuAu), and simple solid solution formation (CuNi). No phase separation tendency in any of the sub-binary systems, which should favour the formation of solid solution NPs. We compare two original and complementary synthesis methods by chemical and physical routes to fabricate FCC HENA with a size between 3 and 10 nm. We also reveal size and compositional effects on the structural properties of these complex nanosystems with aberration-corrected TEM.

2. Experimental

2.1. Physical synthesis: pulsed laser deposition (PLD)

CoNiPt, CoNiPtCu, CoNiPtAu and CoNiPtAuCu HENA were prepared on amorphous carbon film of Mo TEM grids by PLD in a high vacuum chamber (10^{-8} mbar). The experimental set-up described here has been widely used to fabricate bimetallic NPs.[21–25] A typical target–substrate holder configuration and alternating irradiation strategy was used to separately deposit the metals by PLD, using a KrF excimer laser at an emission wavelength of 248 nm. The pulse duration was 25 ns and the laser frequency was set at 5 Hz. The laser irradiation

produced the plasma of the different species with the vaporized atoms subsequently condensing on the substrate placed at a distance of 5 cm from the target. HENA were obtained by alternating irradiation of pure metal targets allowing a composition-controlled synthesis. The deposition rate of each element was controlled by a quartz crystal monitor, which indicates the nominal thickness of deposited materials on the quartz surface, in a continuous thin film approximation. The total nominal thickness of the sample was 1 nm. As the metallic species do not wet the carbon film, nanoparticles were formed instead of continuous thin films and consequently, the average particle thickness was larger than the nominal thickness. During the deposition, the substrate was held at 600 °C using a tantalum filament heated by Joule effect, positioned just behind the TEM grid. We used laser energies of 150 mJ for the gold target and 300 mJ for the other metal targets. These selected energies avoided the formation of micrometric droplets and led to comparable deposition rates for the different metals. The deposition sequence always started with Pt. We used short deposition periods of each metal repeated several times to ensure the homogeneity of the nanoalloys. The total number of pulses on each metal target was fixed in order to reach equiatomic composition.

2.2. Chemical synthesis: hot injection method

HENA were also fabricated in solution using the so-called hot injection method.[26–31] This wet technique is based on the fact that metallic ions in the form of metallic complexes can be reduced to their metallic (zerovalent) state by reacting them with a reducing agent. However, different metallic ions show different reactivities in such reduction reaction and this usually results in core–shell metallic structures, where the most easily reduced metal (thus reacting first) is lying at the core, and the other(s), less easily reduced metals found at the periphery. These reactivity differences can first be overcome by increasing the reaction temperature to such a point that all the metallic salts are reduced at nearly the same rate, the reduction reaction only being limited by the diffusion of the reagents. Second, the heating rate of the reaction media is an equally important parameter. Indeed, if this heating is too slow, the most reactive metal will once again be reduced first, resulting in unwanted core–shell structures. The synthesis protocol thus relies on the simultaneous injection of all the metallic precursors in a solution already heated up to 300 °C where they are homogeneously reduced to induce the nucleation and growth processes. Metallic precursors have been used in the form of acetylacetonate, while the reaction media is composed of benzyl ether (high boiling solvent), 1,2-hexadecanediol (reducing agent) and oleylamine, oleic acid and trioctylphosphine (surfactants). The synthesis was performed under magnetic stirring using a coated magnetic stir bar in the solution and under an argon environment to avoid the presence of oxygen. Detailed information on the synthesis protocols of CoNiPt, CoNiPtCu, and CoNiPtCuAu HENA can be found in the ESI.†

2.3. Aberration-corrected TEM investigations

All TEM investigations were performed with a double aberration-corrected JEOL ARM 200F microscope operated at 200 kV. This microscope is equipped with a high brightness cold field emission source, a JEOL SDD EDX detector and a One

View camera (Gatan Inc.).[21,32] Particle characterizations were performed in both TEM and STEM modes. In the latter, STEM high angle annular dark field (HAADF) images were acquired with spot size setting 8 which corresponds to a probe size of around 0.08 nm. The convergence semi-angle was set to 20.5 mrad while the annular collection angle was set between 68 and 280 mrad in order to minimize diffraction contrast. The elemental composition of the HENA was quantified both on NP assemblies and at single particle level by energy-dispersive X-ray (EDX) spectroscopy. EDX spectra of single NPs were acquired in 1 minute by scanning the electron beam over a rectangular area.

3. Results and discussions

3.1. Synthesis and structural properties of HENA prepared by PLD

Four HENA samples were fabricated by PLD on the carbon film of a TEM grid heated at 600 °C (see Experimental section for details). Fig. 1 and Table 1 show that we successfully obtained ternary CoNiPt (a), quaternary CoNiPtCu (b), quaternary CoNiPtAu (c) and quinary CoNiPtAuCu (d) NPs with a mean size below 5 nm by PLD. The powder electron diffraction patterns of these randomly-oriented NP films were all consistent with solid solutions with FCC structure. This crystal phase is expected for these HENA exclusively made of metals having FCC structures. Moreover, EDX measurements on NP assemblies show that the composition measured over a large area of the sample is close to the equiatomic composition with a deviation below 7% (Table 1). Although these four samples have the same nominal thickness of 1 nm, the mean size of the NPs decreases for the quaternary and quinary nanoalloys with respect to the CoNiPt NPs (Table 1).

The development of nanoalloys requires investigating the atomic structure and composition at the single NP level to evaluate the possible presence of crystal defects and segregation effects as well as to confirm that the crystal structure and the composition are homogeneous throughout the NPs. In that regard, high resolution STEM imaging, EDX chemical mapping and single NP composition

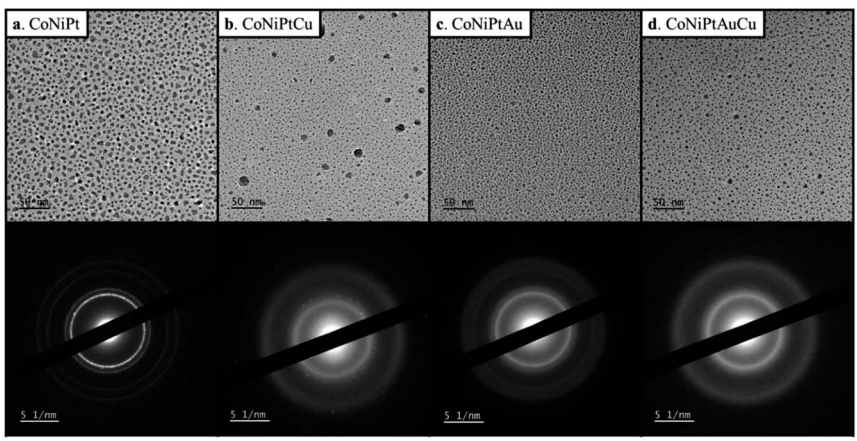

Fig. 1 TEM image and diffraction pattern of (a) CoNiPt; (b) CoNiPtCu; (c) CoNiPtAu; (d) CoNiPtAuCu obtained at 600 °C.

Table 1 Global composition measured by EDX on a large area and mean size of the four HENA prepared by PLD and presented in Fig. 1

	CoNiPt	CoNiPtCu	CoNiPtAu	CoNiPtAuCu
Global composition (at%)	Co = 36.7 Ni = 35.3 Pt = 28.0	Co = 31.7 Ni = 22.0 Pt = 17.1 Cu = 29.2	Co = 31.2 Ni = 29.8 Pt = 17.6 Au = 21.4	Co = 29.6 Ni = 21.9 Pt = 13.0 Cu = 18.4 Au = 17.1
Mean size (nm)	4.8 ± 2.2	1.7 ± 1.0	2.4 ± 1.0	2.9 ± 1.0

measurements were performed on the four samples presented above. As illustrated in Fig. 2, FCC CoNiPt NPs are almost defect free (Fig. 2a and b) and the three elements are homogeneously distributed within the NPs, without segregation (Fig. 2c–f). Quantitative STEM EDX nano-analyses revealed that the nearly equiatomic composition is uniform in all the CoNiPt NPs (Fig. 2g) whatever their size. The composition dispersion is very narrow, 5.6% only on average (Table S1 in the ESI†).

The structural and compositional analysis of the CoNiPtAu and CoNiPtCu nanoalloys confirmed their FCC structure but revealed the presence of a higher density of crystal defects in the NP assemblies in comparison with the ternary HENA (Fig. 3). Together with the NP size reduction, this higher defect density contributes to the diffuse aspect of the signal on the powder electron diffraction pattern of quaternary HENA (Fig. 1b and c). In particular, many twin boundaries and stacking faults are observed in the CoNiPtAu NPs (Fig. 3d and e). It is worth noting that gold NPs frequently adopt multi-twinned structures because the formation energy of stacking faults is low in gold.[33] Therefore, we assume that gold brings these peculiar structural properties to the nanoalloys. One can also

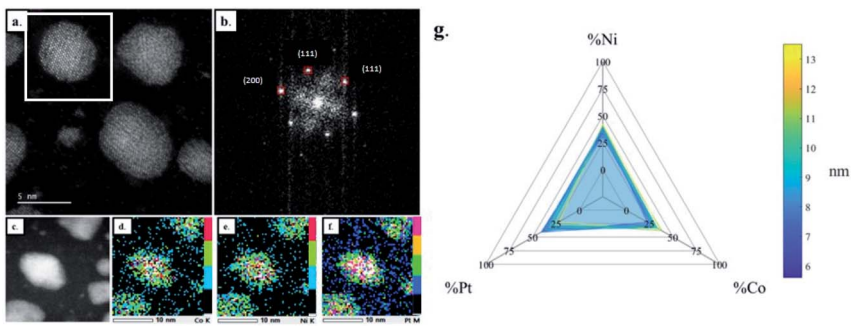

Fig. 2 Structural and compositional analysis of CoNiPt HENA at the single NP level. (a) High resolution STEM-HAADF image of CoNiPt NPs; (b) fast Fourier transform of the NP in the white square in (a) that is oriented along the [101] zone axis; (c–f) EDS chemical mapping of CoNiPt NPs. (c) Reference STEM-HAADF image; chemical elemental maps of (d) Co (using the Co K spectral line); (e) Ni (using the Ni K spectral line); (f) Pt (using the Pt L spectral line). The scale intensity is displayed on the right side of the images. (g) Spider plots showing the composition of single CoNiPt NPs as a function of their size (36 analyzed NPs).

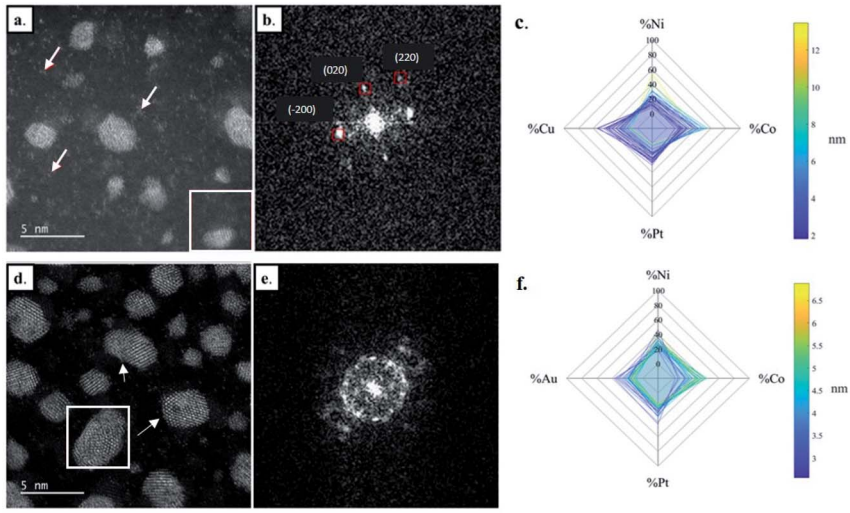

Fig. 3 Structural and compositional analysis of quaternary HENA at the single NP level. (a) High resolution STEM-HAADF image of CoNiPtCu NPs, the white arrows indicate the presence of single Cu atoms and very small nuclei on the carbon substrate; (b) fast Fourier transform of the NP in the white square in (a) that is oriented along the [001] zone axis; (c) spider plots showing the composition of single CoNiPtCu NPs as a function of their size (28 analyzed NPs). (d) High resolution STEM-HAADF image of CoNiPtAu NPs, the white arrows indicate the presence of planar defects in the NPs; (e) fast Fourier transform of the multi-twinned NP in the white square in (d); (f) spider plots showing the composition of single CoNiPtAu NPs as a function of their size (44 analyzed NPs).

assume that Au being the heavier atom, it tends to deform the FCC lattice which favors defect formation. Planar defects are less observed in the CoNiPtCu NPs but we note the presence of many single atoms and very small clusters slowly diffusing on the substrate because of electron irradiation between the well crystallized NPs (Fig. 3a and b). In line with the fact that these single atoms and clusters are not observed in the CoNiPt or CoNiPtAu samples, a Cu signal was detected by EDX when the electron probe was positioned on the substrate.

EDX analysis performed on single NPs shows that the four elements are always present in each NP (Fig. 3c and f), but the dispersion in NP composition is higher than in the CoNiPt system, 8% and 10.6% on average in the CoNiPtAu and CoNiPtCu films, respectively. Interestingly, in both quaternary HENA the composition of NPs is size dependent with an excess of Ni and Co measured in large NPs and conversely more Pt and Au (or Cu) in small NPs (Fig. 3c and f and Tables S2 and S3 in the ESI†).

Finally, the structural and compositional analysis of quinary HENA at the single NP scale revealed that the CoNiPtAuCu nanoalloys combine the structural features observed in the two quaternary nanoalloys (CoNiPtCu and CoNiPtAu). Indeed, many NPs adopt a multi-twinned structure (Fig. 4a and b) and many single atoms are found in between the NPs. The five elements are detected in each NP by EDX (Fig. 4c) and the composition dispersion of NPs is low (only 6.3% on average, see Table S4 in the ESI†). As in the quaternary nanoalloys, there are slight excesses of Ni–Co in large NPs and Cu–Au–Pt in small NPs.

Ostwald ripening is a thermo-activated process that consists of the growth of the larger NPs at the expense of the small ones that shrink. The size-dependent composition of HENA is attributed to an inhomogeneous Ostwald ripening process during their high temperature synthesis. Indeed, as seen in several binary nanoalloys,[34,35] concentration gradients can appear during the synthesis or the annealing of nanoalloys if the metals constituting the NPs have different mobilities. The latter is mainly governed by the desorption energy barrier specific to each metal rather than by atomic diffusion between single NPs on the substrate. The fact that Ni and Co are in excess in large quaternary and quinary nanoalloys means that these two elements are more mobile than Cu, Au and Pt. Consequently, they are more prone to reach large NPs during the Ostwald ripening process. On the contrary, due to the low mobilities of Cu, Au and Pt atoms, these elements are retained in the small NPs that shrink during coarsening. It is worth noting that in equiatomic CoPt nanoparticles, excess of Co is found in large NPs after annealing[35] and the much higher mobility of Pd in equiatomic AuPd nanoparticles leads to complete phase separation after annealing with large Pd and small Au NPs.[34] Therefore, the relative mobility of metals observed in binary nanoalloys fabricated by PLD on amorphous carbon can be used to interpret the effect of Ostwald ripening in HENA.

3.2. Synthesis and structural properties of HENA synthesized by chemical methods

The hot injection protocol was used to fabricate similar ternary, quaternary and quinary nanoalloys (see Experimental section for details). The low resolution TEM image and global electron diffraction of CoNiPt, CoNiPtCu and CoNiPtAuCu nanoalloys are shown in Fig. 5 and the global composition measured by EDX and the average NP size are given in Table 2.

As for the HENA prepared by PLD, all the samples consist of NPs with a FCC structure and a composition close to equiatomic composition with a deviation always below 9.2%. By comparing with the NPs prepared by the physical route, we can assert that the chemical method used leads to bigger NPs than PLD. Chemically prepared NPs are also more monodispersed. Indeed, on average the polydispersity (*i.e.* size dispersion over mean size) is 46% for the NPs fabricated by PLD while it is only 33% for the chemically prepared NPs.

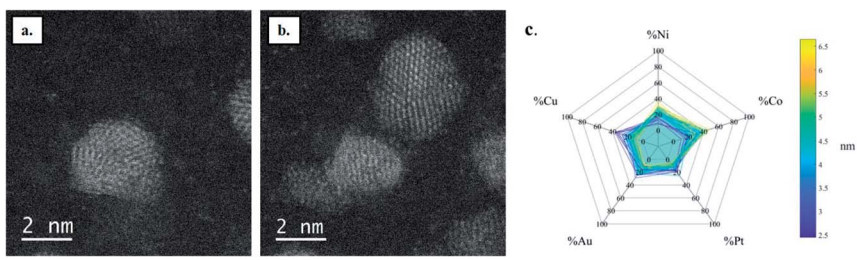

Fig. 4 Structural and compositional analysis of quinary HENA at the single NP level. (a and b) High resolution STEM-HAADF images of multi-twinned CoNiPtAuCu NPs. (c) Spider plots showing the composition of single CoNiPtAuCu NPs as a function of their size (59 analyzed NPs).

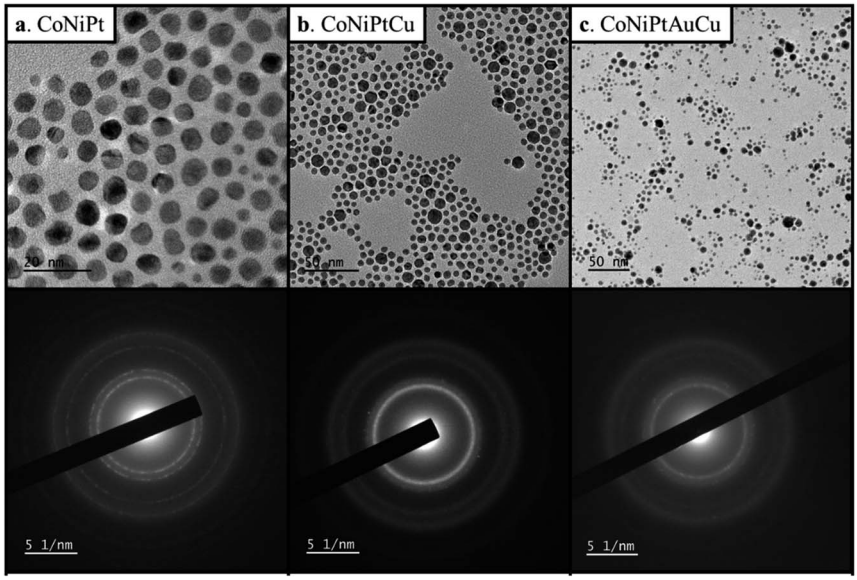

Fig. 5 TEM image and diffraction pattern of (a) CoNiPt, (b) CoNiPtCu and (c) CoNiPtAuCu NPs.

High resolution (S)TEM analysis revealed that crystal defects are rare in the CoNiPt sample where most NPs have a single crystal structure (Fig. 6a), while the great majority of CoPtNiCu and CoPtNiCuAu NPs are multi-twinned nanocrystals (Fig. 6b and c). The increase in crystal defect density with the compositional complexity of the HENA is then confirmed in both chemically and physically prepared NPs.

The EDX analysis of individual quinary HENA (Fig. 6d) revealed that the composition dispersion of NPs is low (only 5.6%, see Table S5 in the ESI†), but we still observed a size dependent composition of NPs. Interestingly, the distribution of elements in the small and large NPs is different from the one revealed in NPs produced by physical synthesis. In the chemically-prepared quinary sample, small NPs present an excess of Co and Pt while large NPs are enriched in Au and Cu. This result highlights the role of the environment on the mobility of metals during Ostwald ripening processes. Indeed, the liquid media, the presence of

Table 2 Global composition measured by EDX on a large area and mean size of the three HENA prepared by chemical methods seen in Fig. 5

	CoNiPt	CoNiPtCu	CoNiPtAuCu
Global composition (at%)	Co = 29.0 Ni = 37.6 Pt = 33.4	Co = 18.6 Ni = 24.3 Pt = 24.3 Cu = 32.8	Co = 10.8 Ni = 19.6 Pt = 24.9 Cu = 26.1 Au = 18.6
Mean size (nm)	5.9 ± 1.2	6.5 ± 1.7	3.7 ± 2.0

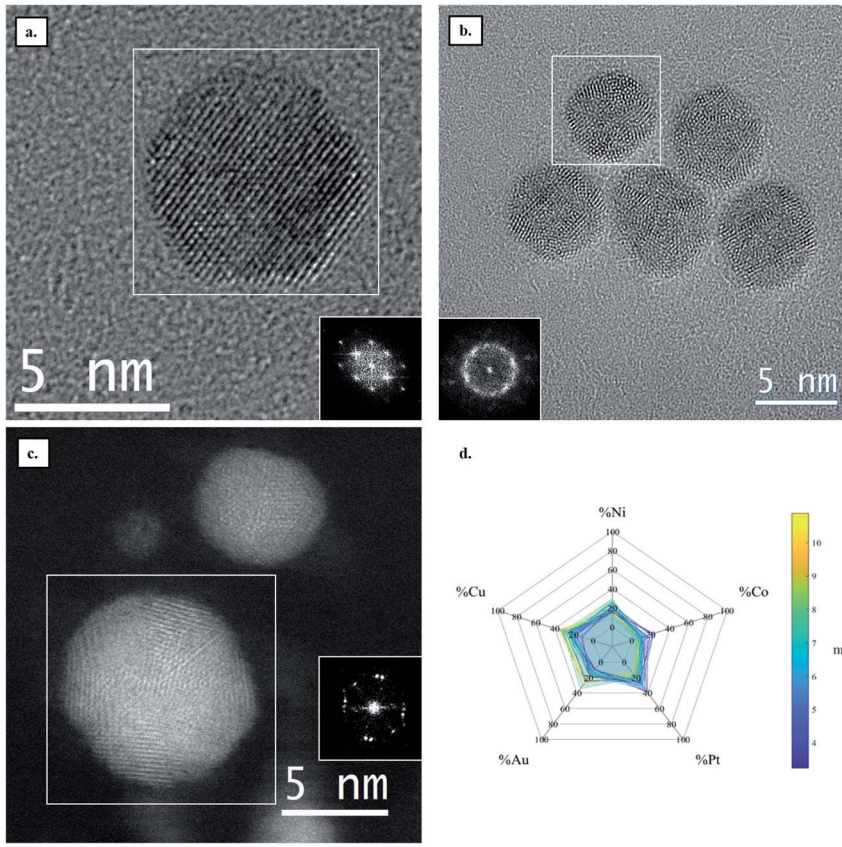

Fig. 6 High resolution (S)TEM images of (a) a monocrystalline CoNiPt NP, (b) multi-twinned CoPtNiCu NPs and (c) multi-twinned CoPtNiAuCu NPs. The Fourier transform of the boxed NP is shown on each image. (d) Spider plots showing the composition of single CoNiPtCuAu NPs as a function of their size (40 analyzed NPs).

ligands at the surface of NPs and the absence of substrate are three parameters that could drastically impact the energy barrier of atom desorption in HENA, leading to different relative mobilities of metals in liquid and in vacuum.

3.3. Vegard law in HENA

The lattice parameter of sub-10 nm binary nanoalloys made of FCC metals usually follows the Vegard law,[23,25] meaning that it roughly corresponds to the weighted mean of the two metals' lattice parameters. If the Vegard law applies to HENA, their lattice parameter would be given by:

$$a_{\mathrm{HENA}} = \sum_i a_i \cdot x_i \quad (1)$$

where a_i and x_i are the lattice parameter and the molar fraction of the metal i, respectively. Interestingly, we observed a significant deviation from the Vegard law in all HENA. As seen in Fig. 7, the lattice parameter measured on the powder diffraction patterns of HENA is systematically higher than the one calculated with

eqn (1) using the composition measured by EDX. This deviation from the Vegard law observed in both physically and chemically prepared NPs, indicates that the lattice distortion mechanisms in nanoalloys containing more than two metals with very different atomic radius are mainly governed by defect formation. This result goes hand in hand with the rise of defect density when the number of elements within the NPs and the resulting strain increase.

3.4. Phase segregation in large HENA

We did not observe any phase segregation in sub-10 nm, but core–shell architectures appeared in larger NPs (Fig. 8 and S1†). Given the larger size of NPs obtained in solution, these large core–shell NPs are mainly observed in chemically prepared samples (Fig. 8a) but we also observed them in samples prepared by PLD on very rare occasions (Fig. 8c). In the CoNiPtCu HENA prepared by wet chemistry, *Z*-contrast STEM HAADF images show a clear contrast enhancement at the edge of big NPs (Fig. 8a and S1†), in line with the higher Pt concentration observed in the same area on the Pt map obtained by EDX (Fig. 8b). Bragg-filtered HRTEM analysis in Fig. 8d–f shows that the phase separation is complete with two distinct FCC structures in the core and the shell of the large NPs. The lattice parameters in the core and in the shell are 3.481 Å and 3.817 Å, respectively. Given the higher lattice parameter of Pt (3.92 Å), this confirms the formation of a Pt-rich shell. Bragg-filtered HRTEM imaging performed by selecting one of the two FCC patterns on the diffractogram of the NPs allows revealing the core of the NPs with a small lattice parameter (Fig. 8e) and the shell of the NPs with a large lattice parameter (Fig. 8f).

As illustrated in Fig. 9, segregation effects are also observed in quinary CoNiPtAuCu nanoalloys. Indeed, the STEM HAADF image and the EDX mapping show that the five elements are homogeneously distributed in small NPs while large NPs have a core rich in AuCu and shell rich in CoNiPt. This result is further

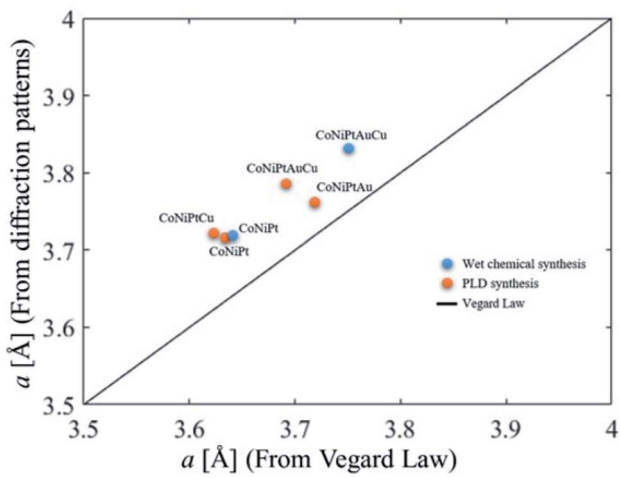

Fig. 7 Lattice parameter of HENA measured on powder diffractions as a function of the lattice parameter calculated with eqn (1) using the composition measured by EDX. The black curve corresponds to the Vegard law.

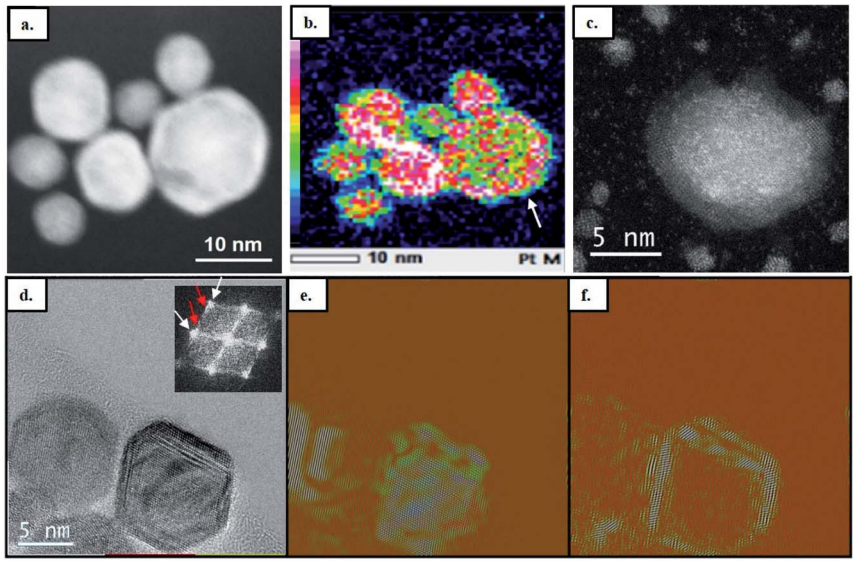

Fig. 8 Large core–shell NPs observed by STEM HAADF in (a) chemically prepared CoNiPtCu HENA. (b) Pt map obtained by STEM-EDX on the NPs shown in (a) (the arrow indicates the Pt-rich shell). The scale intensity is displayed on the left side of the image. (c) Very rare core–shell NPs observed by STEM HAADF in CoNiPtCu HENA fabricated by PLD. (d) HRTEM image of chemically prepared CoNiPtCu NPs showing a core–shell NP with its FFT shown in the inset. The white and red arrows show the Bragg reflections coming from the core and the shell, respectively. Bragg filtered images performed on the HRTEM image seen in (d) by selecting the reflections (e) due to the NP core and (f) due to the NP shell.

demonstrated by the line intensity profile analyses performed on the EDX mappings (Fig. S2†).

It is worth noting that when they were discovered, high entropy alloys in the bulk form were so called because it was thought that the entropy of mixing was high enough to minimize the Gibbs free energy of mixing to therefore stabilize a cubic solid solution rather than demixed structures.[1,2] Indeed, the entropy of mixing increases with the number of elements mixed in the alloys but it decreases when the alloy deviates from the equiatomic composition. In the light of our HENA results, it is tempting to think that the mixing entropy plays an important role. Indeed, the deviation from the equiatomic composition measured in large NPs could thus explain their tendency to form the core–shell configuration. Nevertheless, although elegant, the entropy-driven stabilization of a solid solution in HEA turned out to be an incomplete interpretation since other composition-dependent parameters including the variation of the enthalpy of mixing, the size difference of atoms and the electronic affinity between elements can also significantly affect the crystal phase of HEA.[36] Therefore, the full understanding of the revealed size effect on the nanophase diagram of HENA requires deeper experimental and theoretical investigations.

To further demonstrate this compositional effect on the nanophase diagram HENA, we fabricated $Co_{26}Ni_{32}Pt_{42}$ NPs by PLD, to reveal how an excess of Pt influences the structure of ternary nanoalloys. As illustrated in Fig. 10a, intensity-

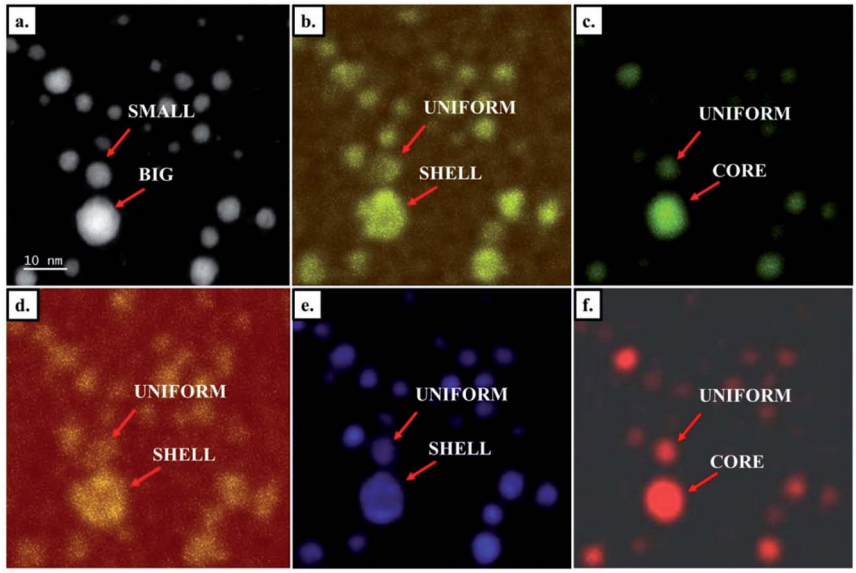

Fig. 9 (a) STEM-HAADF image of CoNiPtAuCu prepared by chemical method. Chemical mapping of (b) Co (K edge), (c) Cu (K edge), (d) Ni (K edge), (e) Pt (L edge) and (f) Au (L edge) performed on the same area.

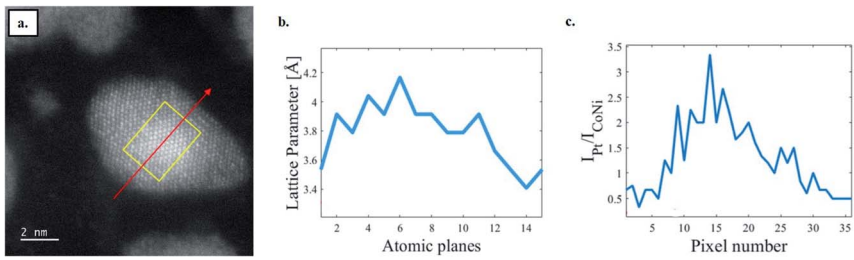

Fig. 10 (a) High resolution STEM-HAADF image of $Co_{26}Ni_{32}Pt_{42}$ NPs made by PLD. (b) Variation of the lattice parameter measured along the yellow rectangle in (a) that is oriented along the [200] direction. (c) Evolution of the ratio between the intensities of the Pt L-peak and the cobalt and nickel K-peaks summed together measured by the EDX line profile along the red arrow in (a).

enhanced areas are observed in the high-resolution STEM-HAADF images of these NPs. The higher intensity of atomic columns goes with the increase of the lattice parameter (Fig. 10b) and the increase of the relative signal of Pt detected by EDX (Fig. 10c) in the core of the NP. Thus, these atomic-scale analyses show that increasing the concentration of Pt by only 10% in CoNiPt NPs leads to the formation of Pt rich cores and highlight the necessity to stay as close as possible to the equiatomic composition to ensure the perfect miscibility of all the metals in FCC nanocrystals.

4. Conclusions

We show that PLD and the hot injection method are efficient fabrication techniques to obtain HENA mixing Co, Ni, Pt, Cu and Au at equiatomic composition in FCC nanocrystals with a size below 10 nm. These two complementary methods allow synthesizing functionalized HENA dispersed in solution or ligand-free HENA supported on various substrates, thus maximizing the application potential of these nano-systems. It also provides the opportunity to study the intrinsic structural properties of HENA. Indeed, although the nucleation and growth processes occur in very different environments, the ternary (CoNiPt), quaternary (CoPtNiCu) and quinary (CoPtNiCuAu) HENA obtained with these two fabrication routes present very similar structural properties. (i) The defect density increases with the compositional complexity of the NPs. (ii) The nanophase diagram of HENA is very sensitive to the composition of the NPs and the obtainment of well-miscible nanoalloys requires staying close to the equiatomic composition. In that regard, the size-dependent composition of HENA driven by the Ostwald ripening that is observed in both physical and chemical syntheses complicates the well-controlled fabrication of HENA with a size over 10 nm. Note that the size-dependent composition of nanoparticles formed under vacuum and in liquid are different due to the effect of the synthesis environment on the mobility of metals. More generally, the fabrication methods developed in this work can be used to explore the almost infinite compositional space of HENA. Moreover, the multi-functionalities of aberration-corrected TEM is the method of choice to study composition and size effects on the structural properties of these complex nanostructures and we hope that these experimental investigations will motivate the development of atomistic simulations[37,38] adapted to the studied HENA that are so far missing to better understand their thermodynamic equilibrium.

Author contributions

D. A., J. N., H. A., C. R. and V. H. conceptualized the experiments. A. B., N. K., C. M. S., N. O. P., A. J., M. T., H. B., J. N., G. W. and D. A. performed the synthesis and TEM analysis. A. B. and D. A. wrote the manuscript. J. N., H. A., C. R. and V. H. reviewed the manuscript. D. A. supervised the project.

Conflicts of interest

There are no conflicts to declare.

Acknowledgements

We gratefully acknowledge the financial support of the Mission for Transversal and Interdisciplinary Initiatives of CNRS (SHENA project) and the Region Ile-de-France (convention SESAME E1845 for the JEOL ARM 200F electron microscope installed at the University Paris Cité).

References

1 B. Cantor, I. Chang, P. Knight and A. Vincent, *Mater. Sci. Eng., A*, 2004, **375**, 213–218.

2 J. W. Yeh, S. K. Chen, S. J. Lin, J. Y. Gan, T. S. Chin, T. T. Shun, C. H. Tsau and S. Y. Chang, *Adv. Eng. Mater.*, 2004, **6**, 299–303.
3 Y. Yao, Z. Huang, P. Xie, S. D. Lacey, R. J. Jacob, H. Xie, F. Chen, A. Nie, T. Pu, M. Rehwoldt, D. Yu, M. R. Zachariah, C. Wang, R. Shahbazian-Yassar, J. Li and L. Hu, *Science*, 2018, **359**, 1489–1494.
4 S. Gao, S. Hao, Z. Huang, Y. Yuan, S. Han, L. Lei, X. Zhang, R. Shahbazian-Yassar and J. Lu, *Nat. Commun.*, 2020, **11**, 1–11.
5 M. Y. Rekha, N. Mallik and C. Srivastava, *Sci. Rep.*, 2018, **8**, 8737.
6 A. Mao, H. Xiang, X. Ran, Y. Li, X. Jin, H. Yu and X. Gu, *J. Alloys Compd.*, 2019, **775**, 1177–1183.
7 Y. Yao, Q. Dong, A. Brozena, J. Luo, J. Miao, M. Chi, C. Wang, I. G. Kevrekidis, Z. J. Ren, J. Greeley, G. Wang, A. Anapolsky and L. Hu, *Science*, 2022, **376**, eabn3103.
8 W. J. Stark, P. R. Stoessel, W. Wohlleben and A. Hafner, *Chem. Soc. Rev.*, 2015, **44**, 5793–5805.
9 D. Wu, K. Kusada, Y. Nanba, M. Koyama, T. Yamamoto, T. Toriyama, S. Matsumura, O. Seo, I. Gueye and J. Kim, *J. Am. Chem. Soc.*, 2022, **144**, 3365–3369.
10 G. Qin, R. Chen, P. K. Liaw, Y. Gao, L. Wang, Y. Su, H. Ding, J. Guo and X. Li, *Nanoscale*, 2020, **12**, 3965–3976.
11 T. Yang, Y. Zhao, Y. Tong, Z. Jiao, J. Wei, J. Cai, X. Han, D. Chen, A. Hu and J. Kai, *Science*, 2018, **362**, 933–937.
12 S. D. Lacey, Q. Dong, Z. Huang, J. Luo, H. Xie, Z. Lin, D. J. Kirsch, V. Vattipalli, C. Povinelli, W. Fan, R. Shahbazian-Yassar, D. Wang and L. Hu, *Nano Lett.*, 2019, **19**, 5149–5158.
13 Y. Xin, S. Li, Y. Qian, W. Zhu, H. Yuan, P. Jiang, R. Guo and L. Wang, *ACS Catal.*, 2020, **10**, 11280–11306.
14 H. Li, Y. Han, H. Zhao, W. Qi, D. Zhang, Y. Yu, W. Cai, S. Li, J. Lai, B. Huang and L. Wang, *Nat. Commun.*, 2020, **11**, 5437.
15 T. Löffler, A. Savan, A. Garzón-Manjón, M. Meischein, C. Scheu, A. Ludwig and W. Schuhmann, *ACS Energy Lett.*, 2019, **4**, 1206–1214.
16 Y. Zhang, D. Wang and S. Wang, *Small*, 2022, **18**, 2104339.
17 P. Xie, Y. Yao, Z. Huang, Z. Liu, J. Zhang, T. Li, G. Wang, R. Shahbazian-Yassar, L. Hu and C. Wang, *Nat. Commun.*, 2019, **10**, 4011.
18 B. Sharma and S. Harini, *Mater. Res. Express*, 2019, **6**, 1165d7.
19 B. Song, Y. Yang, M. Rabbani, T. T. Yang, K. He, X. Hu, Y. Yuan, P. Ghildiyal, V. P. Dravid, M. R. Zachariah, W. A. Saidi, Y. Liu and R. Shahbazian-Yassar, *ACS Nano*, 2020, **14**, 15131–15143.
20 G. Feng, F. Ning, J. Song, H. Shang, K. Zhang, Z. Ding, P. Gao, W. Chu and D. Xia, *J. Am. Chem. Soc.*, 2021, **143**, 17117–17127.
21 D. Alloyeau, T. Oikawa, J. Nelayah, G. Wang and C. Ricolleau, *Appl. Phys. Lett.*, 2012, **101**, 121920.
22 J. Nelayah, N. Nhat Tai, D. Alloyeau, G. Y. Wang and C. Ricolleau, *Nanoscale*, 2014, **6**, 10423–10430.
23 H. Prunier, J. Nelayah, C. Ricolleau, G. Wang, S. Nowak, A.-F. Lamic-Humblot and D. Alloyeau, *Phys. Chem. Chem. Phys.*, 2015, **17**, 28339–28346.
24 V. Pierron-Bohnes, I. Florea, O. Ersen, C. Ulhaq-Bouillet, C. Goyhenex, N. Braidy, C. Ricolleau, Y. Le Bouar and D. Alloyeau, *Cryst. Growth Des.*, 2014, **14**, 2201–2208.

25 D. Alloyeau, C. Langlois, C. Ricolleau, Y. Le Bouar and A. Loiseau, *Nanotechnology*, 2007, **18**, 375301.
26 H. Kobayashi, K. Kusada and H. Kitagawa, *Acc. Chem. Res.*, 2015, **48**, 1551–1559.
27 N. T. K. Thanh, N. Maclean and S. Mahiddine, *Chem. Rev.*, 2014, **114**, 7610–7630.
28 C. M. Da Silva, A. Girard, M. Dufond, F. Fossard, A. Andrieux-Ledier, V. Huc and A. Loiseau, *Nanoscale Adv.*, 2020, **2**, 3882–3889.
29 M. P. Singh and C. Srivastava, *Mater. Lett.*, 2015, **160**, 419–422.
30 C. M. Da Silva, H. Amara, F. Fossard, A. Girard, V. Huc and A. Loiseau, *arXiv*, 2022, preprint, arXiv:2203.03945, DOI: **10.48550/arXiv.2203.03945**.
31 D. Wu, K. Kusada, T. Yamamoto, T. Toriyama, S. Matsumura, I. Gueye, O. Seo, J. Kim, S. Hiroi and O. Sakata, *Chem. Sci.*, 2020, **11**, 12731–12736.
32 A. Nassereddine, Q. Wang, D. Loffreda, C. Ricolleau, D. Alloyeau, C. Louis, L. Delannoy, J. Nelayah and H. Guesmi, *Small*, 2021, **17**, 2104571.
33 I. L. Dillamore and R. E. Smallman, *Philos. Mag.*, 1965, **12**, 191–193.
34 G. Prévot, N. T. Nguyen, D. Alloyeau, C. Ricolleau and J. Nelayah, *ACS Nano*, 2016, **10**, 4127–4133.
35 D. Alloyeau, G. Prévot, Y. Le Bouar, T. Oikawa, C. Langlois, A. Loiseau and C. Ricolleau, *Phys. Rev. Lett.*, 2010, **105**, 255901.
36 E. P. George, D. Raabe and R. O. Ritchie, *Nat. Rev. Mater.*, 2019, **4**, 515–534.
37 S.-P. Ju, I. J. Lee and H.-Y. Chen, *J. Alloys Compd.*, 2021, **858**, 157681.
38 Y.-H. Wen, L. Li, G.-F. Shao and R. Huang, *ACS Appl. Nano Mater.*, 2020, **3**, 5381–5389.